PCCP

ROYAL SOCIETY OF CHEMISTRY

PAPER

Cite this: *Phys. Chem. Chem. Phys.*, 2024, **26**, 1125

The effect of temperature and oxygen partial pressure on the concentration of iron and manganese ions in $La_{1/3}Sr_{2/3}Fe_{1-x}Mn_xO_{3-\delta}$

Sergey S. Nikitin, *[a] Alexander D. Koryakov,[b] Elizaveta A. Antipinskaya,[b] Alexey A. Markov[bc] and Mikhail V. Patrakeev [a]

Received 8th November 2023,
Accepted 7th December 2023

DOI: 10.1039/d3cp05421g

rsc.li/pccp

The oxygen content was measured in cubic perovskite-type $La_{1/3}Sr_{2/3}Fe_{1-x}Mn_xO_{3-\delta}$ (x = 0.1, 0.17, 0.25, and 1/3) in the range of oxygen partial pressure from 10^{-22} to 0.5 atm at 750–950 °C with a step of 50 °C by coulometric titration. Gradual removal of oxygen from the oxides during the measurements was carried out until the stability limit was achieved and the reductive decomposition began. An increase in manganese content was shown to lead to a decrease in the stability of $La_{1/3}Sr_{2/3}Fe_{1-x}Mn_xO_{3-\delta}$ under reducing conditions. The obtained data on oxygen content were used for defect chemistry modeling in the oxides. The enthalpy of the Fe^{3+} to Fe^{4+} and Mn^{3+} to Mn^{4+} oxidation reactions (ΔH_{ox}^0) was determined to be −103.2 ± 0.3 and −250 ± 2 kJ mol^{-1}, respectively, for the x = 0.1 composition, and increased slightly with increasing manganese content. The large difference in ΔH_{ox}^0 determines a strong distinction between the behavior of iron and manganese in perovskite-type oxides. An increase in manganese content in $La_{1/3}Sr_{2/3}Fe_{1-x}Mn_xO_{3-\delta}$ was found to lead to a decrease in the concentration of Fe^{4+} ions, but did not affect the concentration of Fe^{2+} ions. The impact of La/Sr ratio was evaluated by comparison of the obtained data with that for $La_{0.5}Sr_{0.5}Fe_{1-x}Mn_xO_{3-\delta}$, and found to be different for iron and manganese. An increase in lanthanum fraction causes a decrease in the concentration of Fe^{2+} ions and an increase in the concentration of Mn^{2+} under reducing conditions.

1. Introduction

Lanthanum–strontium ferrites $La_{1-x}Sr_xFeO_{3-\delta}$ (LSF) and manganites $La_{1-x}Sr_xMnO_{3-\delta}$ (LSM) with perovskite structure possess mixed conductivity provided by oxygen ions and electron carriers. These oxides have attracted considerable research activities due to their potential application as electrode materials for solid oxide fuel and electrolysis cells (SOFC and SOEC).[1–6]

Manganites are the most widely used cathode materials for high-temperature SOFC.[7] These oxides have high electron conductivity (240 S cm^{-1} at 800 °C for x = 0.3), but negligible oxygen ion conductivity in an ambient atmosphere even at 900 °C.[8] The latter drawback restricting the applicability of manganite for SOFC cathodes at lower temperatures is attributed to the absence of oxygen vacancies in $La_{1-x}Sr_xMnO_{3-\delta}$ at $x < 0.5$.[9] Ferrites, on the otherhand, are characterized by a high concentration of oxygen vacancies and, accordingly, a high level of oxygen-ion conductivity. However, electron conductivity of LSF is markedly lower than that of LSM; moreover, ferrites are less compatible with yttria- and scandia stabilized zirconia (YSZ, ScSZ) electrolytes by thermal expansion coefficient than manganites.[8] There have been attempts to combine iron and manganese in the B-sublattice.[10,11] The main results of these studies have shown that the rate of oxygen transport in $La_{1-x}Sr_xFe_{1-y}Mn_yO_{3-\delta}$ (LSFM) increases with increasing oxygen vacancy concentration, which in turn was conditioned by the x/y ratio. It has been emphasized that "as long as $x \leq y$, the oxygen transport was found to be very slow, while the oxygen transport increased several orders of magnitude when $x > y$".[10] An unexpected conclusion was made as a result of the study of electrical and ionic transport properties of $(La_{0.8}Sr_{0.2})(Mn_{1-y}Fe_y)O_{3\pm\delta}$ (y = 0, 0.2, 0.5, 0.8 and 1). Only the compositions with y = 0 and y = 1 were recommended to be considered as good cathode materials for SOFC application.[12]

Undoubtedly, these results provide useful information about the LSFM system. However, it is difficult to combine this information into a single comprehensive picture elucidating the impact of the cation composition on the properties of the considered oxides. In order to get a deeper insight into the specific properties of the LSFM oxides, it is worth investigating the defect chemistry of the LSFM series using the oxygen content data obtained in wide ranges of oxygen partial pressure and

[a] *Osipyan Institute of Solid State Physics RAS, 142432 Chernogolovka, Moscow District, Russia. E-mail: nikitin@issp.ac.ru*
[b] *Institute of Solid State Chemistry, UB RAS, 620990 Ekaterinburg, Russia*
[c] *Institute of Solid State Chemistry and Mechanochemistry, SB RAS, 630128 Novosibirsk, Russia*

temperature. The results of such a study provide knowledge about the actual oxidation state of both Mn and Fe in the oxide under certain condition, which is necessary not only for the accurate characterization of the materials, but also for the correct interpretation of physical properties, especially electrical conductivity.

This study provides only a step towards understanding the relationship between the composition and properties of LSFM oxides. A detailed and precise measurement of oxygen content in a wide range of oxygen partial pressure has been performed in $La_{1/3}Sr_{2/3}Fe_{1-x}Mn_xO_{3-\delta}$ for x = 0, 0.1, 0.17, 0.25, 1/3. The interval and step of the change in the manganese content were chosen taking into account the results of our previous study in order to provide the necessary and sufficient conditions for identifying the main trends in the variation of oxide properties. The obtained data have been used for defect chemistry modeling in the oxides to derive thermodynamic parameters of defect formation reactions and concentrations of iron and manganese ions in different oxidation states. In our previous work, a similar study for the $La_{0.5}Sr_{0.5}Fe_{1-x}Mn_xO_{3-\delta}$ series was carried out,[13] so, the use of these results for comparison allows evaluating the effect of the La/Sr ratio on the properties of the LSFM system.

2. Experimental

The $La_{1/3}Sr_{2/3}Fe_{1-x}Mn_xO_{3-\delta}$ (x = 0.10, 0.17, 0.25, 1/3) oxides were prepared by solid-state synthesis using La_2O_3 (>99.995%), Fe_2O_3 (>99%), MnO_2 (>99.9%), and $SrCO_3$ (>99.99%) as starting materials. The reagents were annealed at appropriate temperatures to remove adsorbates, then weighted in the required proportions, thoroughly mixed in a mortar with alcohol, dried, and calcined at 1000, 1100, and 1200 °C for 10 hours with intermediate regrinding. The resulting powders of all compositions were pressed into discs and sintered for 10 hours at 1500 °C. The obtained ceramics were milled again for use in studies of structure and oxygen content.

Room-temperature X-ray diffraction (XRD) data were collected on a SmartLab Se Rigaku diffractometer with Cu K_α radiation. The GSAS-II software package was used for the XRD data analysis by the Rietveld method.[14]

The oxygen content in $La_{1/3}Sr_{2/3}Fe_{1-x}Mn_xO_{3-\delta}$ was measured by coulometric titration in the range of oxygen partial pressure (p_{O_2}) from 10^{-20} to 0.5 atm at temperatures of 750–950 °C with a step of 50 °C. A powdered sample of about 0.2 g was placed into a measuring cell of yttria stabilized zirconia (YSZ) with an internal volume of ~0.5 mL, equipped with an electrochemical oxygen pump and sensor. The cell was covered by a YSZ lid with a high-temperature sealant placed between, installed on a holder, and connected electrically. An isolating electrochemical cell of YSZ was mounted over the measuring cell and its internal volume was evacuated and filled with a 50% CO_2/50% O_2 gas mixture. The whole setup was heated up to 1070 °C to seal the measuring cell, after that the temperature was lowered to 950 °C, the isolating cell was closed, and the system was ready for measurements. At p_{O_2} above 10^{-3} atm, coulometric titration was carried out in the isothermal mode *via* a stepwise decrease of the oxygen partial pressure over the sample. At a lower oxygen partial pressure, a temperature step mode was used because it needs less equilibration time.[15] The measurements were carried out with progressive oxygen removal until p_{O_2} ceased to decrease, which signaled the onset of reductive decomposition of the oxide. The experimental data were recorded only after a change in the logarithm of the partial pressure of oxygen over the sample became less than 0.01 per hour. This equilibrium criterion was found to provide good reversibility of the measuring results. More detailed information related to the implementation of coulometric titration can be found elsewhere.[16]

The variation of oxygen content in $La_{1/3}Sr_{2/3}Fe_{1-x}Mn_xO_{3-\delta}$ *versus* temperature in air was carried out on a Setaram TG-DTA 92 thermal analyzer. The measurements were performed in the cooling mode at a rate of 1° min^{-1} after equilibrating the sample with the environment for 5 h. The obtained data were recalculated to $3-\delta$ dependencies *vs.* temperature using reference values of oxygen content acquired from the simulation of coulometric titration data.

3. Methods for oxygen content data analysis

3.1. Defect model

The data of the oxygen content in $La_{1/3}Sr_{2/3}Fe_{1-x}Mn_xO_{3-\delta}$ as a function of oxygen partial pressure were approximated with a point defect model similar to that used for $La_{0.5}Sr_{0.5}Fe_{1-x}Mn_xO_{3-\delta}$.[13] Under experimental conditions, iron and manganese in the perovskite-type oxide can be in 2+, 3+, and 4+ oxidation states. Taking this into account, the composition of the oxides can be written as follows: $La_{1/3}{}^{3+}Sr_{2/3}{}^{2+}(Fe^{2+}Fe^{3+}Fe^{4+})_{1-x}(Mn^{2+}Mn^{3+}Mn^{4+})_xO_{3-\delta}{}^{2-}$. For a more accurate description of the oxygen content data, the defect equilibrium model includes the $\Delta\delta_{ref}$ parameter as an offset of the experimental oxygen data. Since this parameter has no physical sense, it is not shown among the regression results, but is used only for the adjustment of the initial oxygen content data. The adopted model also allows for the possibility that a part of the anionic positions in the oxide can be unavailable for oxygen ions. Several previous studies have demonstrated the efficiency of this parameter use for adequate simulation of the oxygen content data in perovskite-type ferrites.[17,18] The number of unavailable oxygen positions per formula unit of the oxide (w) was assumed to be constant. This is an empirical parameter that can reflect steric disturbance,[17] specific oxygen coordination of cations,[18] or an impact of intercrystalline defects.

The used model assumes that defects in $La_{1/3}Sr_{2/3}Fe_{1-x}Mn_xO_{3-\delta}$ can be formed as a result of four reactions: oxidation of iron and manganese (1, 2), and charge disproportionation on iron and manganese ions (3, 4):

$$2Fe^{3+} + V_O + \frac{1}{2}O_2 \rightleftarrows 2Fe^{4+} + O^{2-};\ K_{ox\,Fe} = \frac{[Fe^{4+}]^2[O^{2-}]}{[Fe^{3+}]^2[V_O]p_{O_2}^{\frac{1}{2}}}, \quad (1)$$

$$2Mn^{3+} + V_O + \frac{1}{2}O_2 \rightleftharpoons 2Mn^{4+} + O^{2-};\ K_{ox\ Mn} = \frac{[Mn^{4+}]^2[O^{2-}]}{[Mn^{3+}]^2[V_O]p_{O_2}^{\frac{1}{2}}}. \quad (2)$$

Here, V_O designates the available oxygen vacancy.

$$2Fe^{3+} \rightleftharpoons Fe^{4+} + Fe^{2+};\ K_{d\ Fe} = \frac{[Fe^{4+}][Fe^{2+}]}{[Fe^{3+}]^2}, \quad (3)$$

$$2Mn^{3+} \rightleftharpoons Mn^{4+} + Mn^{2+};\ K_{d\ Mn} = \frac{[Mn^{4+}][Mn^{2+}]}{[Mn^{3+}]^2}. \quad (4)$$

The temperature dependences of the reaction constants follow a well-known expression:

$$K_i = \exp\left(-\frac{\Delta G_i^0}{RT}\right) = \exp\left(-\frac{\Delta H_i^0}{RT} + \frac{\Delta S_i^0}{R}\right), \quad (5)$$

where R is the molar gas constant, ΔG_i^0, ΔH_i^0, ΔS_i^0 are the standard free Gibbs energy, enthalpy, and entropy changes of the reactions, respectively. Site balance requires:

$$\begin{cases} [Fe^{2+}] + [Fe^{3+}] + [Fe^{4+}] = 1 - x \\ [Mn^{2+}] + [Mn^{3+}] + [Mn^{4+}] = x \end{cases}, \quad (6)$$

$$\begin{cases} [O^{2-}] = 3 - \delta + \Delta\delta_{ref} \\ [V_O] = \delta - w - \Delta\delta_{ref} \end{cases} \quad (7)$$

The charge neutrality condition takes the form:

$$7/3 + 2[Fe^{2+}] + 3[Fe^{3+}] + 4[Fe^{4+}] + 2[Mn^{2+}] + 3[Mn^{3+}] + 4[Mn^{4+}] = 2[O^{2-}]. \quad (8)$$

The joint solution of eqn (1)–(8) gives the relationship between the oxygen partial pressure, the oxygen content in oxides, and the thermodynamic parameters of reactions (1)–(4):

$$16/3 + \frac{(1-x)\cdot(K_{ox\ Fe}\cdot T_s - K_{dFe})}{K_{ox\ Fe}\cdot T_s + \sqrt{K_{ox\ Fe}\cdot T_s} + K_{d\ Fe}} + \frac{x\cdot(K_{ox\ Mn}\cdot T_s - K_{d\ Mn})}{K_{ox\ Mn}\cdot T_s + \sqrt{K_{ox\ Mn}\cdot T_s} + K_{d\ Mn}} = 2(3 - \delta + \Delta\delta_{ref}), \quad (9)$$

where $T_s = \frac{\delta - w - \Delta\delta_{ref}}{3 - \delta + \Delta\delta_{ref}}\cdot\sqrt{p_{O_2}}$.

Eqn (9) was approximated to the experimental data using the Levenberg–Marquardt algorithm of the LMFIT[19] library in a specially written Python program.

3.2. Partial molar enthalpy and entropy of oxygen in $La_{1/3}Sr_{2/3}Fe_{1-x}Mn_xO_{3-\delta}$

Under the condition of thermodynamic equilibrium, the chemical potentials of oxygen in the oxide μ_O and in the gas phase μ_{O_2} are equal:

$$\mu_O = \frac{1}{2}\mu_{O_2}. \quad (10)$$

The expression for the chemical potential of oxygen in the gas phase can be written as:

$$\mu_{O_2} = \mu_{O_2}^0 + RT\ln(p_{O_2}) \quad (11)$$

where $\mu_{O_2}^0$ is the chemical potential of the gas phase oxygen under standard conditions. The chemical potential of oxygen in oxides relative to the standard state in the gas phase $\Delta\mu_O$:

$$\Delta\mu_O = \mu_O - \frac{1}{2}\mu_{O_2}^0 = \frac{1}{2}RT\ln p_{O_2}. \quad (12)$$

The partial molar enthalpy Δh_O and entropy Δs_O of oxygen in the oxide relative to the standard state are related to the respective chemical potential as:

$$\Delta\mu_O = \Delta h_O - T\Delta s_O. \quad (13)$$

The combination of eqn (12) and (13) gives:

$$\Delta h_O = \frac{R}{2}[\partial(\ln(p_{O_2}))/\partial(1/T)]_{\delta,x}, \quad (14)$$

$$\Delta s_O = -\frac{R}{2}[\partial(T\cdot\ln(p_{O_2}))/\partial(T)]_{\delta,x}. \quad (15)$$

3.3. Statistical thermodynamic modeling

The relationships between the partial molar quantities and the thermodynamic parameters of the defect formation reactions in $La_{1/3}Sr_{2/3}Fe_{1-x}Mn_xO_{3-\delta}$ are identical to those derived in:[13]

$$\Delta h_O = (\Delta H_{ox\ Fe} - 2\cdot\Delta H_{d\ Fe}) - \frac{\partial[Fe^{4+}]}{\partial\delta}\cdot\Delta H_{d\ Fe} + \frac{\partial[Mn^{3+}]}{\partial\delta}\cdot\left(\frac{1}{2}(\Delta H_{ox\ Fe} - \Delta H_{ox\ Mn}) + (\Delta H_{d\ Mn} - \Delta H_{d\ Fe})\right) + \frac{\partial[Mn^{4+}]}{\partial\delta}\cdot((\Delta H_{ox\ Fe} - \Delta H_{ox\ Mn}) + (\Delta H_{d\ Mn} - 2\cdot\Delta H_{d\ Fe})), \quad (16)$$

$$\Delta s_O = (\Delta S_{ox\ Fe} - 2\cdot\Delta S_{d\ Fe}) - \frac{\partial[Fe^{4+}]}{\partial\delta}\cdot\Delta S_{d\ Fe} + \frac{\partial[Mn^{3+}]}{\partial\delta}\cdot\left(\frac{1}{2}(\Delta S_{ox\ Fe} - \Delta S_{ox\ Mn}) + (\Delta S_{d\ Mn} - \Delta S_{d\ Fe})\right) + \frac{\partial[Mn^{4+}]}{\partial\delta}\cdot((\Delta S_{ox\ Fe} - \Delta S_{ox\ Mn}) + (\Delta S_{d\ Mn} - 2\cdot\Delta S_{d\ Fe})) - T\cdot s_O^{conf}. \quad (17)$$

Here, $\Delta H_{ox\ Fe}$, $\Delta H_{ox\ Mn}$, $\Delta H_{d\ Fe}$, $\Delta H_{d\ Mn}$, and $\Delta S_{ox\ Fe}$, $\Delta S_{ox\ Mn}$, $\Delta S_{d\ Fe}$, $\Delta S_{d\ Mn}$ are the standard enthalpy and entropy of the corresponding oxidation and charge disproportionation reactions, respectively.

Whereas the expression for the configurational entropy of oxygen s_O^{conf} takes the following form:

$$s_O^{conf} = R \cdot \left(\frac{\partial[Fe^{4+}]}{\partial\delta} \cdot \ln(K_{dFe}) - \frac{\partial[Mn^{3+}]}{\partial\delta} \cdot \ln\left(\sqrt{\frac{K_{ox\ Fe}}{K_{ox\ Mn}}} \cdot \frac{K_{d\ Mn}}{K_{d\ Fe}} \right) - \frac{\partial[Mn^{4+}]}{\partial\delta} \cdot \ln\left(\frac{K_{ox\ Fe}}{K_{ox\ Mn}} \cdot \frac{K_{d\ Mn}}{K_{dFe}^2} \right) + \ln\left(\frac{K_{d\ Fe}{}^2}{K_{ox\ Fe} \cdot \sqrt{p_{O_2}}} \right) \right). \quad (18)$$

4. Results and discussion

4.1. Structure

The powder XRD patterns of $La_{1/3}Sr_{2/3}Fe_{1-x}Mn_xO_{3-\delta}$ shown in Fig. 1 indicate the formation of single-phase oxides with a perovskite-type structure. The inset to the figure shows the 411 Bragg reflections on a larger scale. The reflections demonstrate no signs of splitting associated with rhombohedral lattice distortion, which testifies to the cubic symmetry of the oxides (S.G. $Pm\bar{3}m$), unlike the oxides of $La_{0.5}Sr_{0.5}Fe_{1-x}Mn_xO_{3-\delta}$ series, which have rhombohedral structure (S.G. $R\bar{3}C$). The lattice parameters obtained by the Rietveld refinement of XRD patterns are shown in Table 1 along with the fitting indicators.

In order to elucidate the effect of the manganese content and La/Sr ratio on the crystal lattice, the pseudocubic lattice parameter is shown in Fig. 2(a) as a function of manganese content for $La_{1/3}Sr_{2/3}Fe_{1-x}Mn_xO_{3-\delta}$ and $La_{0.5}Sr_{0.5}Fe_{1-x}Mn_xO_{3-\delta}$. The data for $La_{0.5}Sr_{0.5}Fe_{1-x}Mn_xO_{3-\delta}$ are taken from ref. 13. The observed decrease in the pseudocubic lattice parameter with increasing manganese content is consistent with the substitution

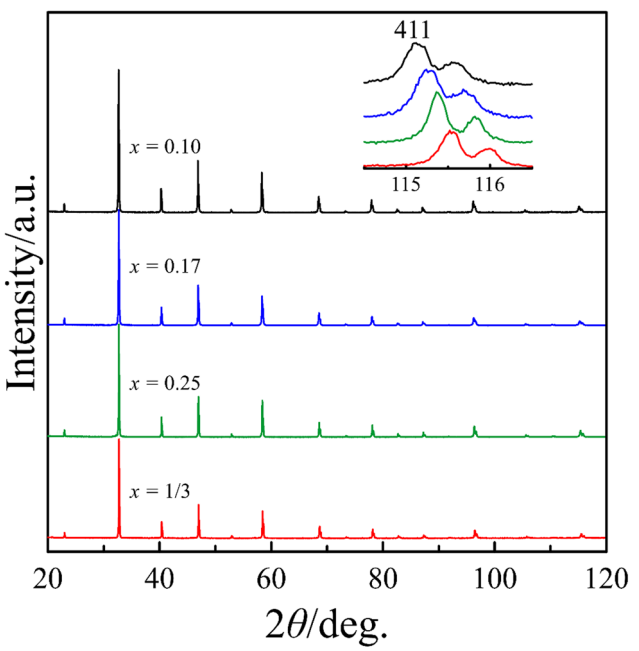

Fig. 1 Room-temperature X-ray powder diffraction patterns of $La_{1/3}Sr_{2/3}Fe_{1-x}Mn_xO_{3-\delta}$ with different manganese content.

Table 1 Unit cell parameter of $La_{1/3}Sr_{2/3}Fe_{1-x}Mn_xO_{3-\delta}$ and characteristics of XRD refinement

x	a, Å	wR, %	wR_{min}, %	GOF
0.10	3.8718(2)	2.92	1.46	1.46
0.17	3.8691(3)	2.83	1.48	1.48
0.25	3.8665(2)	2.80	1.47	1.47
1/3	3.8632(2)	2.91	1.41	1.41

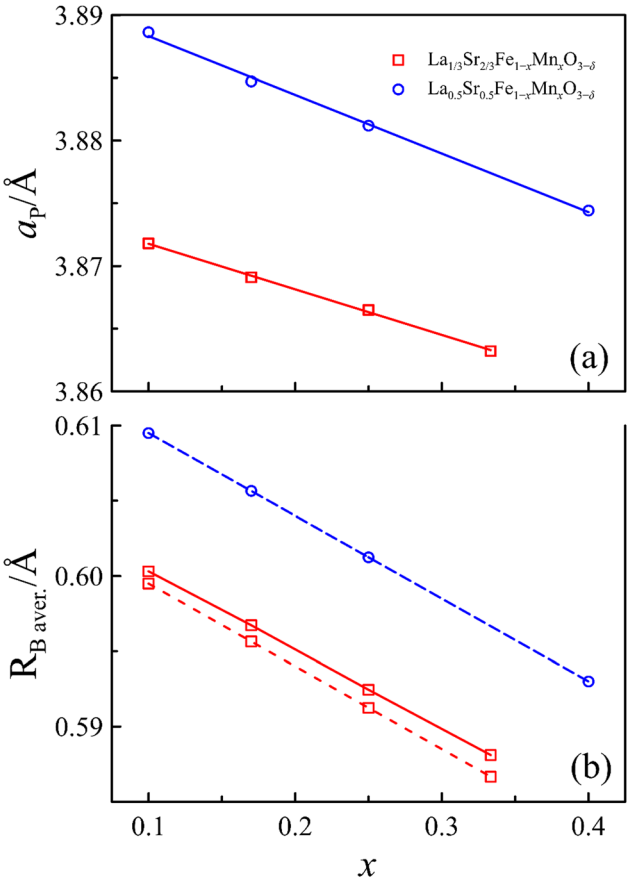

Fig. 2 Quasicubic lattice parameters of $La_{1/3}Sr_{2/3}Fe_{1-x}Mn_xO_{3-\delta}$ and $La_{0.5}Sr_{0.5}Fe_{1-x}Mn_xO_{3-\delta}$ (a), and the average radius of B-site cations (b) as functions of manganese content. Dashed lines demonstrate the results of radius calculation in the assumption of oxygen content 3, whereas calculations with the experimental oxygen content are shown by solid line. Structural data for $La_{0.5}Sr_{0.5}Fe_{1-x}Mn_xO_{3-\delta}$ are taken from ref. 13.

of Fe^{4+} (R_{CN6} = 0.585 Å) with Mn^{4+} (R_{CN6} = 0.530 Å) cations of a smaller radius.[20] Although the radius of Sr^{2+} ions (R_{CN12} = 1.44 Å) is larger than that of La^{3+} ions (R_{CN12} = 1.36 Å), an increase in the strontium content is accompanied by the lattice contraction. The effect can be explained by an increase in the proportion of Fe^{4+} ions, which are smaller than Fe^{3+} ions (R_{CN6} = 0.645 Å).

The plots in Fig. 2(b) demonstrate the effect of manganese content on the average radius of B-site cations in the oxides. The data are calculated under the assumption that the oxygen sublattice is complete at room temperature in air, and manganese is in the oxidation state 4+, in accordance with the formulas: $La^{3+}_{1/3}Sr^{2+}_{2/3}Fe^{3+}_{1-x-p}Fe^{4+}_pMn^{4+}_xO^{2-}_3$ and $La^{3+}_{0.5}Sr^{2+}_{0.5}Fe^{3+}_{1-x-p}Fe^{4+}_pMn^{4+}_xO^{2-}_3$, where p is the

fraction of Fe^{4+} ions in the B sublattice. The portion of Fe^{2+} ions under the considered conditions has been neglected, since the equilibrium constant of the charge disproportionation reaction on iron (3) does not exceed 10^{-5}.[9,13] According to the above formulas, the number of Fe^{3+} and Fe^{4+} cations per formula unit is $[Fe^{3+}] = 0.5$ and $[Fe^{4+}] = 0.5 - x$ for $La_{0.5}Sr_{0.5}Fe_{1-x}Mn_xO_{3-\delta}$, whereas $[Fe^{3+}] = 1/3$ and $[Fe^{4+}] = 2/3 - x$ for $La_{1/3}Sr_{2/3}Fe_{1-x}Mn_xO_{3-\delta}$. The average radius of B-site cations is calculated as: $R_{B\,aver} = [Fe^{3+}]\,R_{Fe3+} + [Fe^{4+}]\,R_{Fe4+} + [Mn^{4+}]\,R_{Mn4+}$. The results are shown in Fig. 2(b) by dashed lines. The estimate does not take into account the larger average radius of A-site cations in $La_{1/3}Sr_{2/3}Fe_{1-x}Mn_xO_{3-\delta}$ and the rhombohedral lattice distortion in $La_{0.5}Sr_{0.5}Fe_{1-x}Mn_xO_{3-\delta}$, which undoubtedly affect the lattice parameters. Nevertheless, the qualitative similarity of the plots in Fig. 2(a) and (b) indicates that the considered change in the average radius of B-site cations gives the main contribution to the change in the unit cell parameter of the oxides.

4.2. Oxygen nonstoichiometry and defect equilibrium

The oxygen content in $La_{1/3}Sr_{2/3}Fe_{1-x}Mn_xO_{3-\delta}$ is shown in Fig. 3 in the form of p_{O_2}–T–$(3-\delta)$ diagrams where the experimental data are represented by symbols. The oxygen removal from the oxide is seen to be accompanied by a decrease in the partial pressure of oxygen over the sample until $3-\delta$ reaches $\sim$2.6, whereas continuation does not result in p_{O_2} decrease, which signals the onset of reductive decomposition of the oxide. A stepwise drop of oxygen content at invariable oxygen partial pressure is highlighted in Fig. 3 by vertical bars. The respective p_{O_2}–T relations are depicted in Fig. 4, which shows the boundary of stability of the $La_{1/3}Sr_{2/3}Fe_{1-x}Mn_xO_{3-\delta}$ oxides under reducing conditions together with similar data for $LaFeO_3$ and $LaMnO_3$ taken for comparison from ref. 21. The stability of $La_{1/3}Sr_{2/3}Fe_{1-x}Mn_xO_{3-\delta}$ is seen to decrease with increasing manganese content, which is consistent with lower stability of $LaMnO_3$ compared to $LaFeO_3$.

The $3-\delta$ isotherms in Fig. 3 have a complicated shape, which depends notably on the manganese content. To estimate better this dependence, the isotherms at 950 °C for the compositions with different manganese content are shown together in Fig. 5. The slope of the curves at oxygen partial pressure above 10^{-5} atm is seen to decrease upon an increase in the manganese content. This part of the isotherms corresponds to the active reduction of Fe^{4+} ions in perovskite-type ferrites *via* reaction (1), whereas manganese under these conditions mainly remains in the oxidation state 4+.[9,13,17,22] Therefore, a decrease in the slope should indicate a decrease in the Fe^{4+} fraction, which is consistent with the above expression $[Fe^{4+}] = 2/3 - x$. An increase in the slope of the curves in the p_{O_2} range between 10^{-12} and 10^{-5} atm upon an increase in the manganese content is natural to associate with the predominant contribution of the Mn^{4+} reduction *via* reaction (2) to the redox processes occurring under these conditions. A further increase in the slope of the isotherms at oxygen partial pressure below 10^{-12} atm is attributed to a progressive reduction of both iron and manganese to the 2+ oxidation state.[9,22] It is noteworthy that all the curves intersect at oxygen content $\sim$2.667 that corresponds to the average oxidation state of B-site 3+ cations. This can serve as a confirmation of the correctness of experimental data adjustment on oxygen content, and allows using

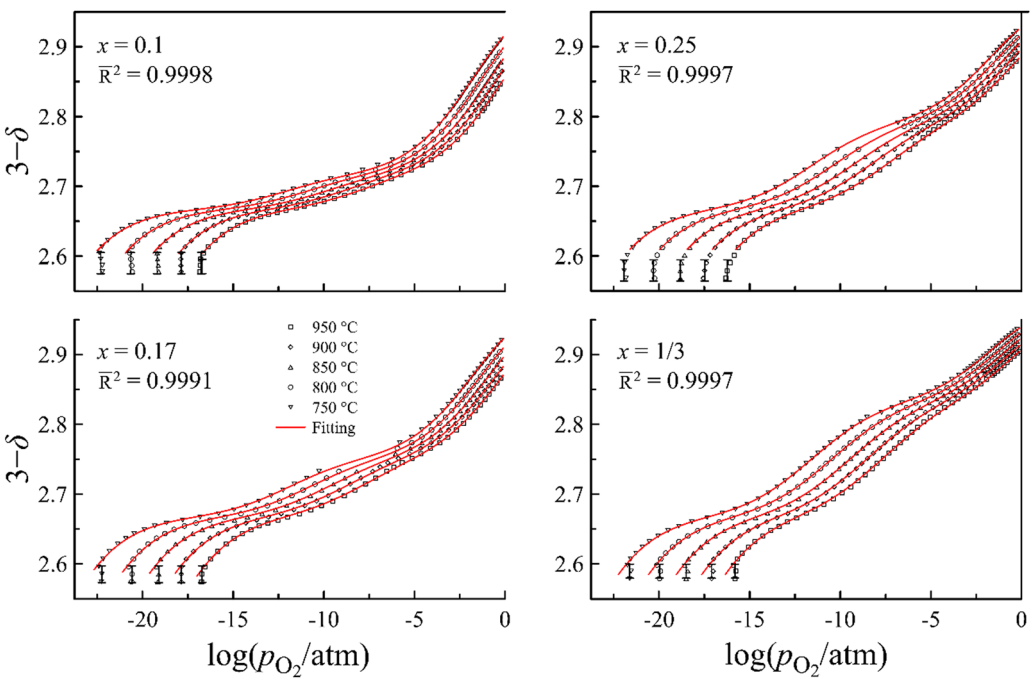

Fig. 3 Oxygen content in $La_{1/3}Sr_{2/3}Fe_{1-x}Mn_xO_{3-\delta}$ as a function of oxygen partial pressure at different temperatures. Experimental data are presented by symbols, the results of model calculation according to eqn (9) are presented by solid lines. A decrease in oxygen content at permanent p_{O_2}, highlighted by vertical bars, indicate reductive decomposition.

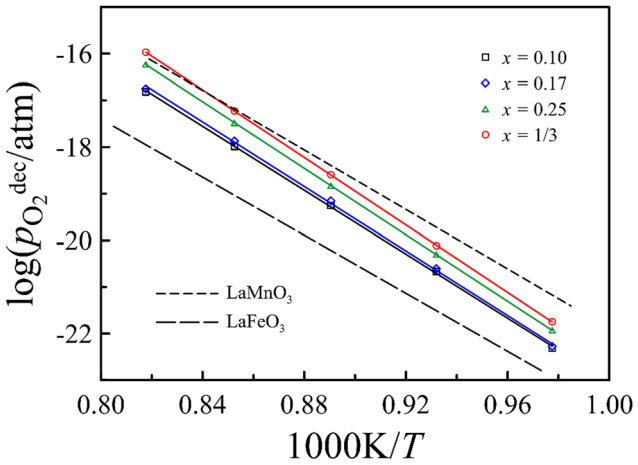

Fig. 4 Boundary of stability of $La_{1/3}Sr_{2/3}Fe_{1-x}Mn_xO_{3-\delta}$ under reducing conditions. p_{O_2}–T data corresponding to the onset of reductive decomposition are taken from Fig. 3. Respective data for $LaFeO_3$ and $LaMnO_3$ are taken for comparison from ref. 21.

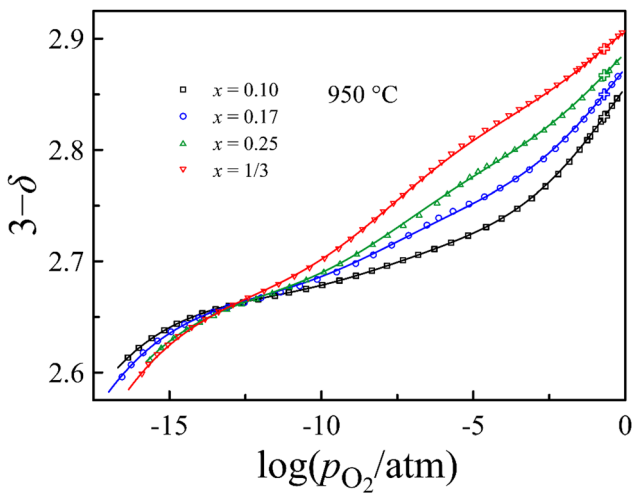

Fig. 5 Isotherms of oxygen content in $La_{1/3}Sr_{2/3}Fe_{1-x}Mn_xO_{3-\delta}$ at 950 °C. The cross-like symbols indicate oxygen content in air to be used as reference.

the results for the reference. The cross-like symbols in Fig. 5 designate the oxygen content at 950 °C and p_{O_2} corresponding to air. These $3-\delta$ values are obtained by interpolation of the experimental data and are intended to be used for the calculation of oxygen content data from the results of thermogravimetric measurements, according to the following expression:

$$3-\delta(T) = 3-\delta_{ref} + \frac{\Delta W(T)\cdot M_{ref}}{W_{ref}\cdot M_O}. \quad (19)$$

$3-\delta(T)$ and $3-\delta_{ref}$ in eqn (19) designate the oxygen content in the oxide at a current temperature and under reference conditions (950 °C, air), respectively; $\Delta W(T)$ is the increment of the sample weight relative to the reference value; W_{ref} is the reference weight of the sample; M_{ref} is the molar mass of the sample under reference conditions; M_O is the oxygen molar mass.

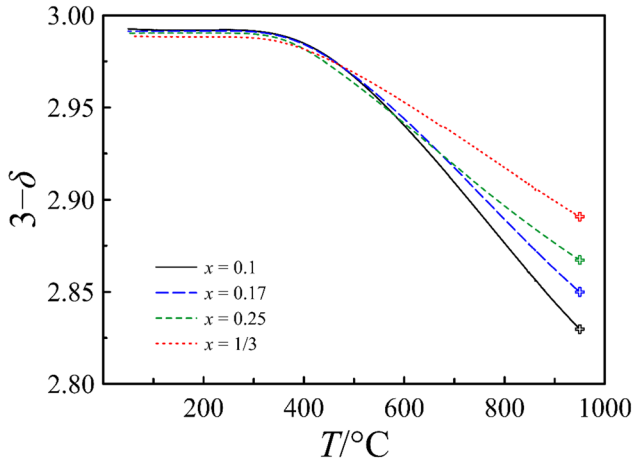

Fig. 6 Oxygen content in $La_{1/3}Sr_{2/3}Fe_{1-x}Mn_xO_{3-\delta}$ as a function of temperature in the air atmosphere. Lines present the results calculated from thermogravimetric data using the reference oxygen content values taken from Fig. 5 and indicated by the cross-like symbols. The circles present oxygen content values at 750, 800, 850, and 900 °C obtained by interpolation of data in Fig. 5.

The oxygen content in $La_{1/3}Sr_{2/3}Fe_{1-x}Mn_xO_{3-\delta}$ as a function of temperature in Fig. 6 shows that slow cooling in air to room temperature does not lead to the complete filling of anion positions with oxygen, therefore the average radius of the B-site cations in Fig. 2 is underestimated. However, the maximum deviation of the oxygen content from 3, observed for the composition $x = 1/3$ is only 0.012. Therefore, the use of experimental data on the oxygen content in oxides in the calculation gives only a slight correction in the average radius of the B-site cations, as shown in Fig. 2 by a solid line. The results in Fig. 5 and Fig. 6 indicate that Mn^{4+} ions are more stable to reduction than Fe^{4+}, which favors higher oxygen content in the $La_{1/3}Sr_{2/3}Fe_{1-x}Mn_xO_{3-\delta}$ oxides with higher manganese content at high temperatures under oxidizing conditions. Nevertheless, a decrease in p_{O_2} down to $\sim 10^{-12}$ atm is accompanied by a greater removal of oxygen from the oxides with higher manganese content, therefore, the overall amount of oxygen that releases in this state, starting from room temperature in air, practically does not depend on the manganese content.

The results of calculations using eqn (9), shown in Fig. 3 by solid lines, demonstrate good agreement with the experimental data. The proximity of the adjusted R-squared values to unity also confirms the adequacy of the defect equilibrium model. The thermodynamic parameters of the defect formation reactions obtained in the calculations are summarized in Table 2. Although the $La_{1/3}Sr_{2/3}Fe_{1-x}Mn_xO_{3-\delta}$ oxides comprise iron and manganese in one sublattice, these elements demonstrate thermodynamic parameters close to those they have in perovskite structured ferrites and manganites, respectively.[23,24] For instance, the absolute value of the enthalpy of manganese oxidation reaction (2) is more than twice higher than that of iron oxidation reaction (1). Thus, the enthalpy and entropy of defect formation reactions have reasonable values that change monotonically with increasing manganese concentration.

Table 2 Thermodynamic parameters of defect equilibrium in $La_{1/3}Sr_{2/3}Fe_{1-x}Mn_xO_{3-\delta}$

	$x = 0.10$	$x = 0.17$	$x = 0.25$	$x = 1/3$
$\Delta H^0_{ox\,Fe}$ (kJ mol^{-1})	−103.2 ± 0.3	−99.4 ± 0.7	−94.1 ± 0.6	−93.2 ± 0.6
$\Delta S^0_{ox\,Fe}$ (J mol^{-1}K^{-1})	−70.4 ± 0.2	−66.9 ± 0.6	−63.3 ± 0.5	−63.0 ± 0.5
$\Delta H^0_{d\,Fe}$ (kJ mol^{-1})	119.7 ± 0.3	118 ± 1	116 ± 1	116 ± 1
$\Delta S^0_{d\,Fe}$ (J mol^{-1}K^{-1})	0[a]	0[a]	0[a]	0[a]
$\Delta H^0_{ox\,Mn}$ (kJ mol^{-1})	−250 ± 2	−242 ± 3	−249 ± 1	−236 ± 1
$\Delta S^0_{ox\,Mn}$ (J mol^{-1}K^{-1})	−109 ± 1	−102 ± 1	−112 ± 1	−98 ± 1
$\Delta H^0_{d\,Mn}$ (kJ mol^{-1})	116 ± 2	102 ± 2	86 ± 2	85 ± 1
$\Delta S^0_{d\,Mn}$ (J mol^{-1}K^{-1})	42.6 ± 0.8	33.8 ± 0.8	18.3 ± 0.6	20.0 ± 0.6
$w \times 10^3$	34.3 ± 0.5	35.4 ± 0.6	41.7 ± 0.7	37.9 ± 0.5

[a] Statistically insignificant.

Considering the regression parameters in Table 2, it should be noted that the values of w although low, exceed the experimentally determined oxygen deficiency in the oxides at room temperature in Fig. 6, which varies from 0.007 to 0.012. On the other hand, fixing the parameter w in the model at such low values significantly worsens the description of experimental data. Therefore, the parameter w probably denotes a certain asymptotic point for reducing oxygen deficiency in the oxide, applicable for the experimental temperature range. Now it is not possible to identify the factors responsible for the change in this parameter upon cooling to room temperature.

To clarify better the redox behavior of iron and manganese, it is worth considering the values of equilibrium constants of the ion pair interaction. These constants, derived from the thermodynamic parameters in Table 2, are shown in Fig. 7 for 950 °C as a representative example.

The constant of iron oxidation reaction (1) for all compositions is about five orders of magnitude lower than the respective constant of manganese oxidation reaction (2). This characterizes Fe^{4+} ions as much more easily reducible than Mn^{4+}. Accordingly, heating leads to the greater oxygen removal the less manganese the oxide contains, in agreement with the data in Fig. 6. It should be noted, that although both enthalpy and entropy of oxidation reactions in Table 2 changes notably (5–10%) as manganese content increases from 0.1 to 1/3, mutual compensation of their contributions results in an insignificant dependence of the free Gibbs energy, and, respectively, the equilibrium constants of reactions (1) and (2) on the manganese content, as can be seen in Fig. 7.

Fig. 7 depicts also the reaction constants for the $La_{0.5}Sr_{0.5}Fe_{1-x}Mn_xO_{3-\delta}$ compositions taken for comparison from ref. 13. Comparing the values of the constants implies that the concentrations of Mn^{2+} ions in $La_{1/3}Sr_{2/3}Fe_{1-x}Mn_xO_{3-\delta}$ over the entire oxygen partial pressure range should be lower, while the concentrations of Mn^{3+} ions should be higher than those in $La_{0.5}Sr_{0.5}Fe_{1-x}Mn_xO_{3-\delta}$. As for iron, $La_{1/3}Sr_{2/3}Fe_{1-x}Mn_xO_{3-\delta}$ should contain more Fe^{2+} ions and less Fe^{4+} ions than $La_{0.5}Sr_{0.5}Fe_{1-x}Mn_xO_{3-\delta}$.

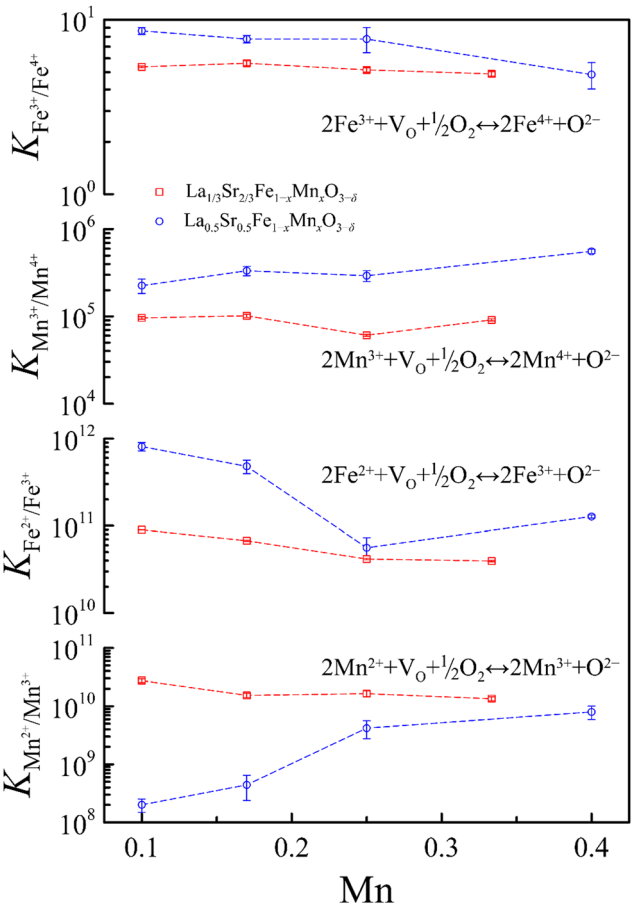

Fig. 7 Equilibrium constants for specified defect formation reactions in $La_{1/3}Sr_{2/3}Fe_{1-x}Mn_xO_{3-\delta}$ as a function of manganese content at 950 °C. The values of error bars are obtained based on the errors of thermodynamic parameters from Table 2. The lines are a guide for the eye.

4.3. Thermodynamic quantities

Fig. 8 and Fig. 9 exhibit the partial molar enthalpy and entropy of oxygen in $La_{1/3}Sr_{2/3}Fe_{1-x}Mn_xO_{3-\delta}$, which are calculated directly from the experimental data according to eqn (14) and (15) and shown by dots, as well as the results of statistical thermodynamic modeling with eqn (16) and (17), which are shown by lines. It is worth noting that the sets of results obtained from the experimental data and by model calculations are in good agreement, which indicates the reliability of the thermodynamic parameters of the defect formation reactions in Table 2.

The idealized curve of partial molar enthalpy of oxygen *versus* oxygen content in perovskite-type ferrites with only iron

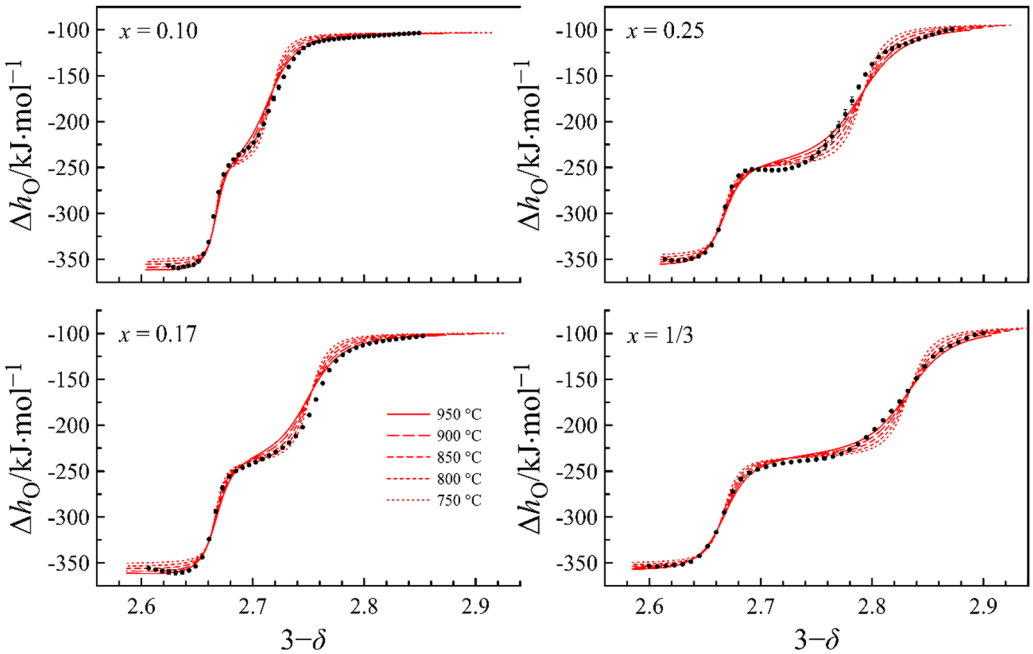

Fig. 8 Partial molar enthalpy of oxygen in $La_{1/3}Sr_{2/3}Fe_{1-x}Mn_xO_{3-\delta}$ as a function of oxygen content in oxides. The results calculated from experimental data with eqn (14) are shown by symbols with error bars. The results obtained by statistical thermodynamic modeling using eqn (16) are presented by solid lines.

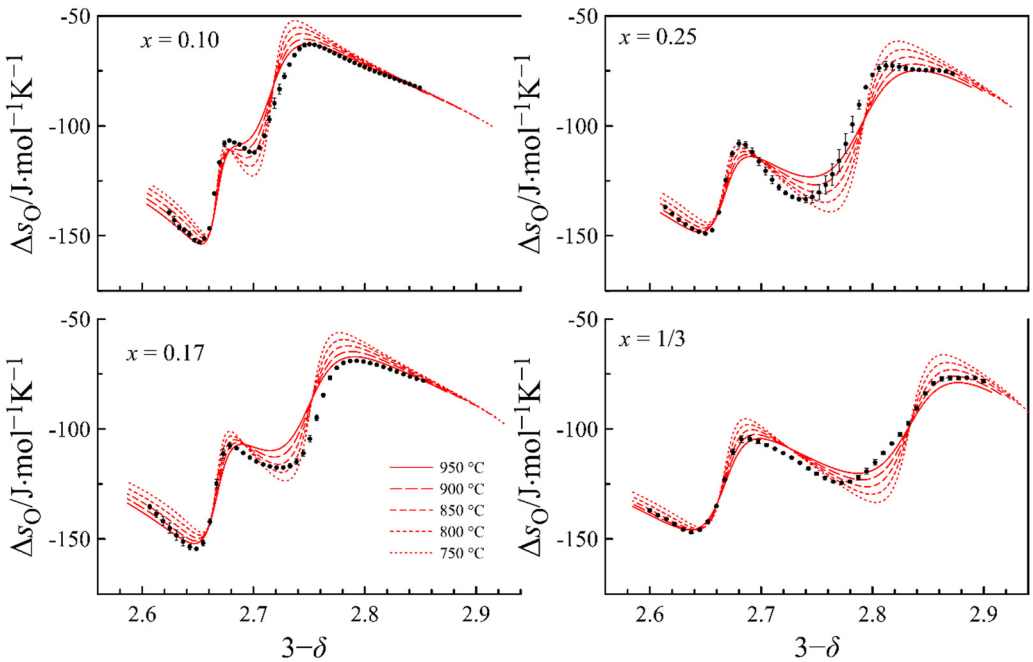

Fig. 9 Partial molar entropy of oxygen in $La_{1/3}Sr_{2/3}Fe_{1-x}Mn_xO_{3-\delta}$ as a function of oxygen content in oxides. The results calculated from experimental data with eqn (15) are shown by symbols with error bars. The results obtained by statistical thermodynamic modeling using eqn (17) are presented by solid lines.

in the B-sublattice has a simple shape and consists of three elements.[25,26] The first one is an upper horizontal branch at high oxygen content, the level of which corresponds to the enthalpy of the Fe^{3+} to Fe^{4+} oxidation reaction. The second one is a lower horizontal branch at low oxygen content, the level of which corresponds to the enthalpy of the Fe^{2+} to Fe^{3+} oxidation reaction. The third element is a vertical line, which connects two branches at oxygen content corresponding to the average oxidation state of iron 3+. Partial substitution of iron with manganese results in distortion of this curve shape, as is seen

in Fig. 8. At $x = 0.1$ the vertical line is slightly sloped, and a kind of bump appears on this part of the curve. As manganese content increases, the bump gradually transforms into a plateau, the level of which corresponds to the enthalpy of the Mn^{3+} to Mn^{4+} oxidation reaction. Thus, complex shapes of the curves of partial molar enthalpy of oxygen reflect a multi-stage reduction/oxidation process of $La_{1/3}Sr_{2/3}Fe_{1-x}Mn_xO_{3-\delta}$. Similarly, Fig. 9 demonstrates the shape evolution of the partial molar entropy of oxygen attributed to the growing contribution of the paired Mn^{3+}–Mn^{4+} interaction to redox processes upon an increase in manganese content in the oxide.

4.4. Defect concentrations

In Fig. 10, the concentration of iron and manganese in different oxidation states is shown as a function of oxygen partial pressure at different temperatures for the compositions $x = 0.1$ and $x = 1/3$ in order to trace the effect of manganese content. In addition, similar data for $La_{0.5}Sr_{0.5}Fe_{1-x}Mn_xO_{3-\delta}$, $x = 0.1$ taken from[13] are included in the figure to reveal the impact of the La/Sr ratio.

According to Fig. 10, the main distinction of manganese from iron is better stability of the former in the oxidation state 4+, associated with a significantly lower enthalpy of reaction (2) compared to (1). This feature prevents the formation of oxygen vacancies in $La_{1-x}Sr_xMnO_{3+d}$ above 10^{-5} atm even at 1000 °C for the compositions with $x \leq 0.5$.[9] This very feature is responsible for low oxygen conductivity of the lanthanum strontium manganites, which limits the performance of these materials as SOFC cathodes at temperatures below 900 °C.[27] Another distinctive manganese quality is the ability to coexist in different oxidation states in close concentrations, in contrast to iron. This quality is determined by a considerably larger

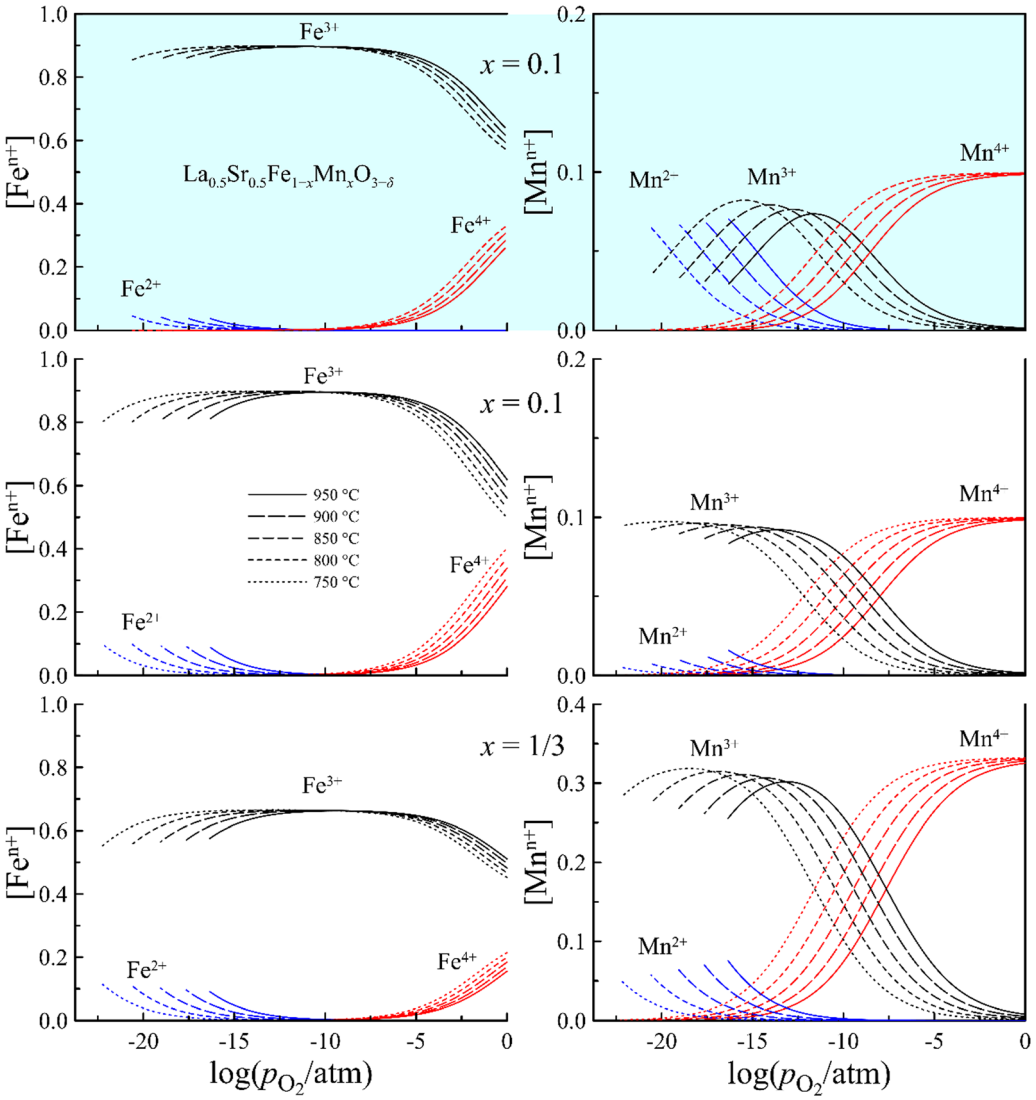

Fig. 10 Concentration of iron and manganese ions in different oxidation states in $La_{1/3}Sr_{2/3}Fe_{1-x}Mn_xO_{3-\delta}$ as a function of oxygen partial pressure at different temperatures. Data for $x = 0.1$ and $x = 1/3$ are presented as examples. The upper panel, highlighted by color, presents similar data for $La_{0.5}Sr_{0.5}Fe_{1-x}Mn_xO_{3-\delta}$ ($x = 0.1$) taken for comparison from ref. 13.

equilibrium constant of disproportionation reaction for Mn (4) than for Fe (3). A simple estimate using eqn (5) shows that at 950 °C $K_{d\,Mn}$ is $\sim 1.9 \times 10^{-3}$ whereas is $K_{d\,Fe}$ is $\sim 7.7 \times 10^{-6}$. Another feature in Fig. 10 that is worth drawing attention to is that an increase in the manganese content in $La_{1/3}Sr_{2/3}Fe_{1-x}Mn_xO_{3-\delta}$ from 0.1 to 1/3 results in a decrease in the Fe^{4+} concentration under oxidizing conditions but does not affect the Fe^{2+} concentration under reducing conditions. As for the effect of La/Sr ratio, it is different for iron and manganese. In particular, an increase in the La fraction in the A-sublattice from 1/3 to 0.5 at $x = 0.1$ causes a considerable decrease in the percentage of the Fe^{2+} ions and a respective increase that of Mn^{2+} under reducing conditions, in agreement with the expectations that arose when considering the equilibrium constants. It is clearly seen in Fig. 10 that at low oxygen partial pressure the concentration of Mn^{2+} can exceeds that of Mn^{3+} in $La_{0.5}Sr_{0.5}Fe_{1-x}Mn_xO_{3-\delta}$, whereas in $La_{1/3}Sr_{2/3}Fe_{1-x}Mn_xO_{3-\delta}$ at the same manganese content it remains several times lower than the concentration of Mn^{3+}. The mechanisms of the revealed interrelations are not evident and deserve separate studies.

5. Conclusion

Perovskite-type oxides $La_{1/3}Sr_{2/3}Fe_{1-x}Mn_xO_{3-\delta}$ (x = 0.1, 0.17, 0.25, and 1/3) were synthesized by the conventional solid-state method and characterized by X-ray diffraction as having a cubic structure. The unit cell parameter of the oxides was found to decrease with an increase in manganese content that is attributed to a smaller ion radius of Mn^{4+} compared to Fe^{4+}. The oxygen content was measured in $La_{1/3}Sr_{2/3}Fe_{1-x}Mn_xO_{3-\delta}$ by thermogravimetry as a function of temperature in air and by coulometric titration as a function of oxygen partial pressure at different temperatures. The stability of the oxides under reducing conditions, which was determined during the measurements, was found to decrease with increasing manganese content. Modeling of experimental data on oxygen content allowed obtaining the standard enthalpy and entropy of defect formation reactions and calculating the concentrations of iron and manganese cations in different oxidation states. According to the obtained results, the impact of the manganese substitution for iron on the properties of $La_{1/3}Sr_{2/3}Fe_{1-x}Mn_xO_{3-\delta}$ is mainly due to better stability of Mn^{4+} ions against the reduction than that of Fe^{4+} and the ability of manganese to reside in the oxide in 4+, 3 +, and 2+ oxidation states in comparable concentrations. A comparison with similar data for $La_{0.5}Sr_{0.5}Fe_{1-x}Mn_xO_{3-\delta}$ showed that an increase in the lanthanum content favors higher concentration of Mn^{2+} and lower concentration of Fe^{2+} under reducing conditions.

Conflicts of interest

There are no conflicts to declare.

Acknowledgements

The authors are grateful to the Russian Science Foundation (project 21-79-30051) for the support of this work.

References

1 B. Pan, H. Miao, F. Liu, M. Wu and J. Yuan, *Int. J. Hydrogen Energy*, 2023, **48**, 11045–11057.
2 K. K. Hansen, *Solid State Ionics*, 2020, **344**, 115096.
3 M. Pidburtnyi, B. Zanca, C. Coppex, S. Jimenez-Villegas and V. Thangadurai, *Chem. Mater.*, 2021, **33**, 4249–4268.
4 A. Shi, Y. Kong, Z. Li, Y. Wang, S. Fan and Z. Jin, *Int. J. Electrochem. Sci.*, 2023, **18**, 100126.
5 J. Hong, S. J. Heo and P. Singh, *Appl. Surf. Sci.*, 2020, **530**, 14725.
6 R. Tian, J. Fan, Y. Liu and C. Xi, *J. Power Sources*, 2008, **185**, 1247–1251.
7 S. P. Jiang, *J. Mater. Sci.*, 2008, **43**, 6799–6833.
8 C. Sun, R. Hui and J. Roller, *J. Solid State Electrochem.*, 2010, **14**, 1125–1144.
9 J. Mizusaki, N. Mori, H. Takai, Y. Yonemura, H. Minamiue, H. Tagawa, M. Dokiya, H. Inaba, K. Naraya, T. Sasamoto and T. Hashimoto, *Solid State Ionics*, 2000, **129**, 163–177.
10 L. Mikkelsen, I. G. K. Andersen and E. M. Skou, *Solid State Ionics*, 2002, **152–153**, 703–707.
11 S. Kato, D. Kikawa, M. Ogasawara, Y. Moriya, M. Sugai and S. Nakata, *Solid State Ionics*, 2005, **176**, 1377–1381.
12 M. Petitjean, G. Caboche, E. Siebert, L. Dessemond and L.-C. Dufour, *J. Eur. Ceram. Soc.*, 2005, **25**, 2651–2654.
13 S. S. Nikitin, A. A. Markov, O. V. Merkulov, A. V. Chukin and M. V. Patrakeev, *Dalton Trans.*, 2021, **50**, 17967–17980.
14 B. H. Toby and R. B. Von Dreele, *J. Appl. Crystallogr.*, 2013, **46**, 544–549.
15 M. H. R. Lankhorst, H. J. M. Bouwmeester and H. Verweij, *Solid State Ionics*, 1997, **96**, 21–27.
16 M. V. Patrakeev, I. A. Leonidov and V. L. Kozhevnikov, *J. Solid State Electrochem.*, 2011, **15**, 931–954.
17 A. A. Markov, S. S. Nikitin, B. V. Politov, E. V. Shalaeva, A. P. Tyutyunnik, I. A. Leonidov and M. V. Patrakeev, *J. Alloys Compd.*, 2021, **875**, 160051.
18 O. V. Merkulov, E. N. Naumovich, M. V. Patrakeev, A. A. Markov, E. V. Shalaeva, V. V. Kharton, E. V. Tsipis, J. C. Waerenborgh, I. A. Leonidov and V. L. Kozhevnikov, *J. Solid State Electrochem.*, 2018, **22**, 727–737.
19 Non-Linear Least-Squares Minimization and Curve-Fitting for Python, **https://lmfit.github.io/lmfit-py** (accessed 1 November 2023).
20 R. D. Shannon, *Acta Crystallogr., Sect. A: Cryst. Phys., Diffr., Theor. Gen. Crystallogr.*, 1976, **32**, 751–767.
21 T. Nakamura, G. Petzow and L. J. Gaukler, *Mat. Res. Bull.*, 1979, **14**, 649–659.
22 J. Mizusaki, M. Yoshihiro, S. Yamauchi and K. Fueki, *J. Solid State Chem.*, 1985, **58**(2), 257–266.
23 J. Cheng, A. Navrotsky, X.-D. Zhou and H. U. Anderson, *Chem. Mater.*, 2005, **17**, 2197–2207.
24 M. Takacs, M. Hoes, M. Caduff, T. Cooper, J. R. Scheffe and A. Steinfeld, *Acta Mater.*, 2016, **103**, 700–710.
25 J. Mizusaki, M. Yoshishiro, S. Yamauchi and K. Fueki, *J. Solid State Chem.*, 1987, **67**, 1–8.
26 C. Y. Park and A. J. Jacobson, *J. Electrochem. Soc.*, 2005, **152**, J65–J73.
27 D. A. Osinkin, *Electrochim. Acta*, 2021, **372**, 137858.

